INVESTIGATION OF ELECTROCHEMICAL CHARACTERISTICS of α-Na_xMnO_2 CATHODES FOR SODIUM-ION BATTERIES

Van Ky Nguyen[1,2,*], Dinh Thao Vu[1], Trung Son Luong[1], Dinh Lam Vu[2], Van Nghia Nguyen[3]

[1]*Faculty of Physics and Chemical Engineering, Le Quy Don Technical University*

[2]*Graduate University of Science and Technology, Vietnam Academy of Science and Technology*

[3]*Institute of Architecture, Construction, Urban and Technology, Hanoi Architectural University*

Abstract

P2 and O3 layered structure materials have large potential for application as cathodes for sodium-ion batteries. This article presents the research results on the electrochemical properties of layered structure α-Na_xMnO_2 (x = 0.7-1.0) cathode materials synthesized via the sol-gel method. The α-Na_xMnO_2 cathode materials were characterized by X-ray diffraction (XRD) to determine their crystal structure, scanning electron microscopy (SEM) to analyze their morphology, and energy-dispersive X-ray spectroscopy (EDX) to assess their elemental composition. The electrochemical properties of α-Na_xMnO_2 materials were investigated using CR2032 coin cells, in which the cathodes were fabricated from the synthesized α-Na_xMnO_2 materials. The α-Na_xMnO_2 cathode material exhibited the highest initial charge-discharge capacity at a rate of 0.1 C when x = 1.0, with values of 168.43 $mAh.g^{-1}$ and 165.18 $mAh.g^{-1}$ in the first cycle, respectively. However, the capacity declined significantly after 10 cycles and reached only about 50.02% of its initial value after 50 cycles. The composition with the highest cycling stability was $Na_{0.8}MnO_2$ (x = 0.8), maintaining 63.37% of its initial capacity after 50 cycles. Electrochemical impedance spectroscopy (EIS) and cyclic voltammetry (CV) measurements were conducted using an Ivium potentiostat to evaluate the electrochemical properties of the synthesized materials. The α-$NaxMnO_2$ material demonstrates strong potential as a cathode candidate for sodium-ion batteries.

Keywords: *Sodium-ion battery; sodium manganese oxide; cathode materials; sol-gel method.*

1. Introduction

Electric vehicles are becoming increasingly popular as an environmentally friendly means of transport, helping to reduce emissions in big cities. The strong development of electric vehicles leads to a huge demand for batteries. Today, electric cars and mobile devices predominantly rely on lithium-ion batteries. Consequently, the

[*] Corresponding author, email: kyanh@lqdtu.edu.vn

DOI: 10.56651/lqdtu.jst.v3.n02.1053.pce

raw materials required for producing lithium-ion batteries are becoming increasingly scarce and expensive. This has spurred scientists to relentlessly explore alternative energy sources to meet the growing demand for electric vehicles. Sodium-ion batteries have attracted significant research interest and are emerging as promising candidates to replace lithium-ion batteries. They have advantages: (i) an abundant sodium supply obtained from seawater and salt mines that can be refined at a much lower cost than lithium; (ii) a low standard redox potential of $E°_{(Na^+/Na)}$ = -2.71 V relative to the standard hydrogen electrode in aqueous solutions; (iii) low toxicity, and ease of synthesis [1]-[3]. However, the larger ionic radius of sodium compared to lithium results in a reduced intercalation efficiency during the charge-discharge process. Therefore, it is imperative to investigate materials with crystal lattice structures that can effectively intercalate sodium ions to ensure optimal battery performance [1]-[5].

Sodium manganese oxide materials can effectively intercalate sodium ions, making them very promising for cathode materials for sodium-ion batteries. However, sodium manganese oxides exhibit various phase structures that depend on the initial molar ratio of Na to Mn and the synthesis temperature. For instance, a Na:Mn ratio of (0 to 0.40):1 at temperatures below 750°C results in the formation of $Na_{0.40}MnO_2$ and Mn_2O_3 phases. A ratio of (0.40 to 0.44):1 under the same temperature conditions yields both $Na_{0.40}MnO_2$ and $Na_{0.44}MnO_2$ phases. When the Na:Mn ratio ranges from 0 to 0.44:1 at temperatures above 750°C, the predominant phase is $Na_{0.44}MnO_2$ ($Na_4Mn_9O_{18}$), accompanied by Mn_2O_3. Moreover, when the Na:Mn ratio ranges from 0.44 to 0.70:1, temperatures below 630°C lead to the formation of $Na_{0.44}MnO_2$ and α-$Na_{0.70}MnO_{2+y}$ (where $y \leq 0.05$), whereas temperatures above 630°C favor $Na_{0.44}MnO_2$ and β-$Na_{0.70}MnO_{2+y}$. For Na:Mn ratios between 0.70 and 1.00:1, temperatures exceeding 850°C yield β-$Na_{0.70}MnO_{2+y}$ and β-$NaMnO_2$ phases; temperatures in the range of approximately 630°C to 850°C result in β-$Na_{0.70}MnO_{2+y}$ and α-$NaMnO_2$; and temperatures below 600°C produce α-$Na_{0.70}MnO_{2+y}$ along with Na_3MnO_4. Furthermore, when the Na:Mn ratio exceeds 1.00, synthesis at temperatures between approximately 630°C and 850°C leads to α-$NaMnO_2$ and Na_3MnO_4 phases, while temperatures above 850°C result in β-$NaMnO_2$ and Na_3MnO_4 [6]. In this study, we chose the synthesis temperature of Na_xMnO_2 material as 700°C to form the desired phases α-Na_xMnO_2.

The various phase structures of sodium manganese oxides capable of sodium ion intercalation vary widely, leading to notable variations in cycle stability and achieved capacity. For example, the material $Na_{0.44}MnO_2$ ($Na_4Mn_9O_{18}$) features a tunnel structure with an orthorhombic crystal lattice belonging to the Pbam space group, as indicated by

JCPDS card No #27-0750, and reported as a cathode material with charge-discharge capacities ranging from approximately 80 $mAh.g^{-1}$ to 121 $mAh.g^{-1}$ [7]-[12]. Another example is $Na_{0.7}MnO_2$, it depends on the synthesis conditions, which may exhibit either a crystal structure corresponding to the orthorhombic system (β-$Na_{0.7}MnO_2$, according to JCPDS card No #27-0752) or a hexagonal prismatic form (α-$Na_{0.7}MnO_{2+y}$, with $y \leq 0.05$, as per JCPDS card #27-0751), yielding charge-discharge capacities of approximately 100 $mAh.g^{-1}$ to 160 $mAh.g^{-1}$ [13]-[19]. Furthermore, the material $Na_{1.0}MnO_2$ may exhibit various crystal structures, depending on the synthesis conditions. It achieves capacities ranging from 120 $mAh.g^{-1}$ to 190 $mAh.g^{-1}$ [20]-[22].

In addition, during the charge–discharge process, structural transitions occur among different polymorphic forms of sodium manganese oxide, leading to variations in cycle stability depending on the molar ratio of Na: Mn. For instance, the molar ratio Na:Mn > 0.44 and sodium manganese oxide have the layered structure form, which have a shift between the Pn and On forms. Specifically, Pn and On (n = 2,3) phases refer to the spatial positions within the triangular prism and octahedral frameworks, where sodium ions are accommodated and can migrate to adjacent octahedral sites or along the prism structure. In other words, layered-structure Na_xMnO_2 materials P2-type and O3-type have exhibited the ability to intercalate and extract sodium ions from the crystal lattice during charge-discharge cycles [17], [23], [24]. To gain a comprehensive understanding and determine an optimal initial molar ratio of Na:Mn, we synthesized Na_xMnO_2 (x = 0.7-1.0) materials using the sol-gel method and investigated the material's properties, with specific results presented in the following sections.

2. Experiments

2.1. Synthesis of materials

The α-Na_xMnO_2 materials (x = 0.7-1.0) were synthesized using the sol-gel method through two heat treatment steps at 550°C and 700°C. The chemicals used were CH_3COONa (Sigma-Aldrich, ≥ 99%), $Mn(CH_3COO)_2.4H_2O$ (Sigma-Aldrich, ≥ 99%), and citric acid (Sigma-Aldrich). The α-Na_xMnO_2 materials were synthesized according to the following steps:

Initially, chemicals were weighed on an analytical balance with an accuracy of 10^{-3} g so that the molar ratio of Na:Mn:Citric acid was x:1:1, and an extra 5% of Na compared to the calculated amount. This was done to obtain Na_xMnO_2 materials (x = 0.7-1.0) after synthesis.

Next, CH_3COONa was dissolved in distilled water to prepare a 1 mol/L CH_3COONa solution, while $Mn(CH_3COO)_2.4H_2O$, along with citric acid, were dissolved in distilled water to obtain a 1 mol/L $Mn(CH_3COO)_2$ solution.

Subsequently, the sodium acetate solution was slowly introduced into the manganese and citric acid mixture.

The resulting blend was then stirred and heated at 90°C for 24 hours using a magnetic stirrer, resulting in the formation of a sol-gel precursor.

This precursor underwent calcination at 550°C for 3 hours, followed by a second calcination at 700°C for 20 hours to yield the α-Na_xMnO_2 materials. Both calcination processes were carried out in air at a heating rate of 5°C/min and cooled naturally in the furnace.

Finally, the obtained materials were stored in a desiccator for further processes, such as structural, morphological, and compositional analysis, as well as battery fabrication for evaluating electrochemical properties.

2.2. Sample preparation for electrochemical characterization analysis

The α-Na_xMnO_2 materials (x = 0.7-1.0) were fabricated into electrodes with a composition of 80% by weight Na_xMnO_2, 10% Carbon Black (Sigma-Aldrich, ≥ 95%), and 10% Polyvinylidene Fluoride (PVDF) (Sigma-Aldrich, ≥ 99%). Electrodes were fabricated as follows: First, 0.05 g of PVDF was weighed and dissolved in 5 g of 1-methyl-2-pyrrolidone (Sigma-Aldrich, ≥ 99%); Second, 0.40 g of Na_xMnO_2 and 0.05 g of Carbon Black were ground thoroughly in an agate mortar; Third, the two mixtures were transferred into a 50 mL glass beaker and stirred using a magnetic stirrer for 1 hour. Fourth, the resulting electrode slurry was coated onto aluminum foil using a TOB electrode coater, and the coating system was adjusted so that the material layer on the aluminum foil was 20 ± 5 μm thick. Fifth, Aluminum foil was coated with an electrode material mixture that was dried in a vacuum oven at 80°C under a pressure of about 200 mmHg for 24 hours. Sixth, the electrode layer on the aluminum foil was pressed with a roll press to ensure an electrode thickness of around 20 μm. Finally, the coated material on aluminum foil was cut using a cutter to form circular positive electrodes with a diameter of 16 mm, and the electrodes were assembled with Na anode in a glove box to fabricate CR2032-type cells.

2.3. Material characterization

The crystal structure of α-Na_xMnO_2 was determined using X-ray diffraction (XRD) on a Siemens D5005 diffractometer. In this analysis, Cu-Kα1 radiation (λ = 1.54 Å) was

employed over a 2θ range of 10-70° with a step size of 0.05°. The morphology of the α-Na_xMnO_2 materials was investigated using scanning electron microscopy (SEM) on a JEOL JSM-6490 instrument, and their composition was analyzed via energy dispersive X-ray spectroscopy (EDX) using the same machine.

The electrochemical performance of the α-Na_xMnO_2 material was evaluated using cyclic voltammetry (CV) and electrochemical impedance spectroscopy (EIS) on an IVIUM multi-function electrochemical meter. The CV scan was conducted over a voltage range of 1.5 V to 4.0 V at a scanning rate of 0.1 $mV.s^{-1}$. The electrochemical impedance spectra of the Na_xMnO_2 samples were measured over a frequency range from 1 MHz to 0.1 Hz, with an applied AC voltage amplitude of 10 mV. During the measurement, the working electrode was connected to the battery's positive terminal, while the counter and reference electrodes were connected to the negative terminal. Additionally, its charge-discharge capacity was measured across a voltage range of 1.5 V to 4.0 V at various current densities using a NEWARE battery testing system (GCD).

Electrochemical measurements were carried out on CR2032-type sodium-ion batteries. In these cells, α-Na_xMnO_2 served as the cathode, while sodium foil functioned as the anode. A polypropylene (PE) membrane was employed as the separator, and the electrolyte consisted of a 1 M $NaClO_4$ solution dissolved in an equal-volume mixture of ethylene carbonate (EC) and diethylene carbonate (DEC). The CR2032 coin cells were assembled in a glove box where oxygen and moisture levels were maintained below 0.1 ppm, and they were allowed to stabilize for 24 hours before testing.

3. Results and discussions

3.1. Morphological and structural characterization

Figure 1 illustrates the X-ray diffraction (XRD) patterns of the synthesized α-Na_xMnO_2 samples, with sodium content ranging from x = 0.7 to 1.0. Notably, the $Na_{0.7}MnO_2$ sample exhibits distinct and well-defined diffraction peaks, which closely correspond to the standard reference card JCPDS #27-0751 for α-Na_xMnO_2. This phase is attributed to a hexagonal crystal system with the space group P63/mmc, characterized by a layered P2-type structure [17]. The diffraction peaks, marked by asterisks (*) in the figure, corresponding to the planes (002), (004), (100), (102), (103), and (104), appearing at 2θ values of 15.79°, 31.82°, 36.13°, 39.66°, 43.68°, and 49.05°, respectively. The lattice parameters, automatically refined using HighScore Plus software, are determined to be a = b = 2.874 Å, c = 11.122 Å, with angles α = β = 90° and γ = 120°, indicating a symmetrical hexagonal configuration.

The X-ray diffraction (XRD) pattern of the synthesized $Na_{1.0}MnO_2$ material, presented in Fig. 1, reveals well-defined diffraction peaks that can be compared with the standard JCPDS card No #25-0845 for α-$NaMnO_2$. This phase belongs to the monoclinic crystal system, space group C2/m, and the layered O3-type structure [17], [20], [25]. Its characteristic diffraction peaks, marked with a hashtag symbol (#), correspond to 2θ angles of 16.65°, 33.74°, 34.47°, 37.68°, 42.66°, 57.19°, and 58.68°, which are indexed to the (001), (002), (200), (-202), (111), (-113), and (202) crystal planes, respectively. Additionally, diffraction peaks observed at 15.85°, 36.13°, and 39.67° highlighted with an asterisk (*) are attributed to the α-$Na_{0.70}MnO_2$ phase, corresponding to the (002), (100), and (102) planes. Therefore, the synthesized $Na_{1.0}MnO_2$ material primarily consists of the α-$NaMnO_2$ phase, with a minor α-$Na_{0.70}MnO_2$ phase component, consistent with the phase diagram of Na_xMnO_2 at the synthesis temperature of 700°C [6].

The diffraction patterns of the $Na_{0.8}MnO_2$ and $Na_{0.9}MnO_2$ samples, as shown in Fig. 1, also indicate that the synthesized material comprises two distinct phases: α-$Na_{0.7}MnO_2$, marked by an asterisk (*) at characteristic diffraction peaks, and α-$NaMnO_2$, identified by a hashtag symbol (#) at their corresponding diffraction positions. When the peak intensities are normalized, as presented in Fig. 1, it becomes evident that increasing the initial Na:Mn ratio from 0.7 to 1.0 leads to a gradual decrease in the diffraction peaks of the α-$Na_{0.7}MnO_2$ phase most notably at approximately 15.8°, corresponding to the (002) crystal plane, while they nearly vanish at other positions. Meanwhile, diffraction peaks associated with the α-$NaMnO_2$ phase are nearly absent at a Na:Mn ratio of 0.7, begin to emerge at 0.8 (at positions marked with a hashtag), and become significantly more pronounced at ratios of 0.9 and 1.0. This trend is entirely consistent with the phase diagram of Na_xMnO_2 synthesized at temperatures below 700°C [6].

The morphological characteristics of α-$NaxMnO_2$ samples were investigated using scanning electron microscopy (SEM), with the findings illustrated in Fig. 2. At a magnification of 10,000 times, the SEM images of samples revealed that the crystal grains possessed polyhedral shapes and exhibited dimensions ranging from approximately one to several micrometers.

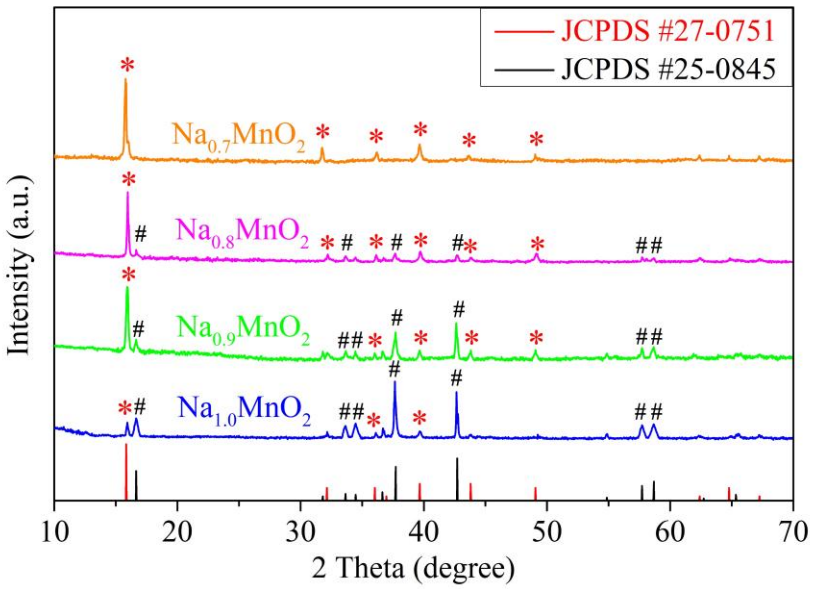

Fig. 1. X-ray diffraction (XRD) patterns of α-Na_xMnO_2 materials.

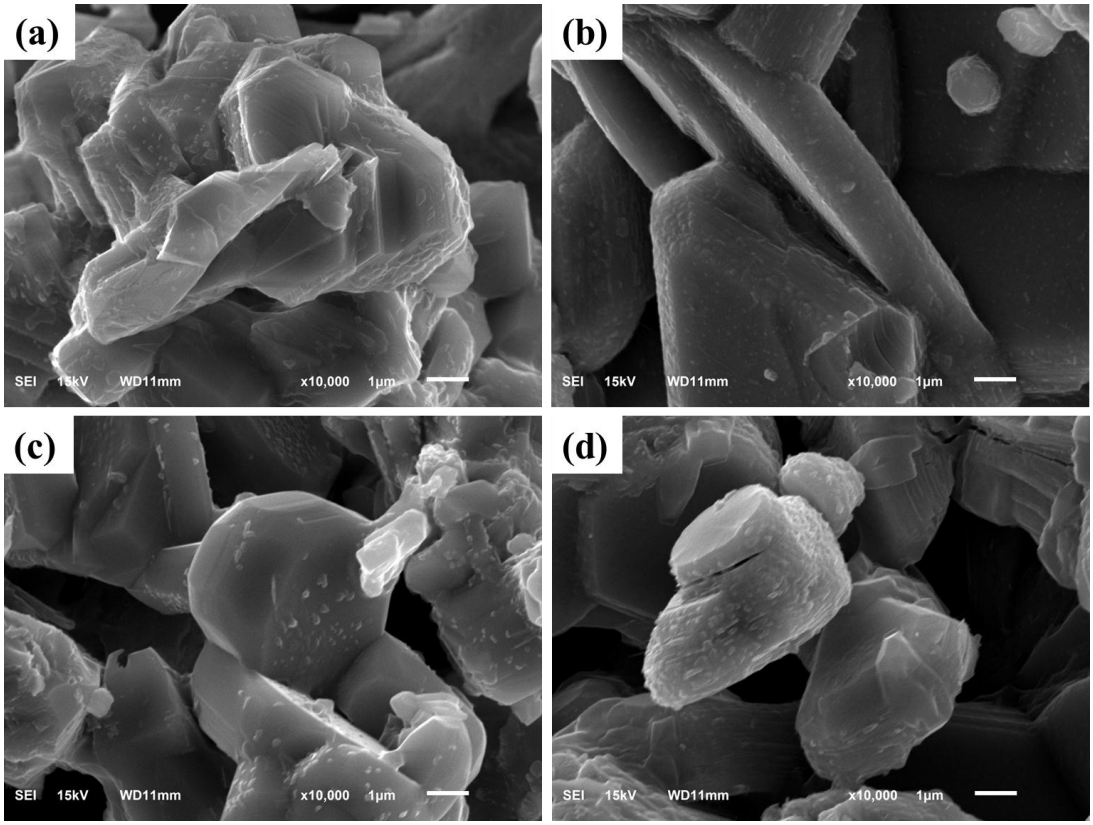

Fig. 2. SEM images of α-Na_xMnO_2 materials:
(a) $Na_{0.7}MnO_2$; (b) $Na_{0.8}MnO_2$; (c) $Na_{0.9}MnO_2$; (d) $Na_{1.0}MnO_2$.

The elemental composition of the synthesized α-Na_xMnO_2 specimens was assessed by energy-dispersive X-ray spectroscopy (EDX), with spectra presented in Figs. 3a-d corresponding to nominal $Na_{0.7}MnO_2$, $Na_{0.8}MnO_2$, $Na_{0.9}MnO_2$, and $Na_{1.0}MnO_3$, respectively. Quantitative evaluation of the EDX data provided both mass and atomic percentages, which were subsequently employed to recalculate the material stoichiometries, yielding refined formulas of $Na_{0.702}MnO_2$, $Na_{0.803}MnO_2$, $Na_{0.901}MnO_2$, and $Na_{1.03}MnO_2$. The minor discrepancies relative to the theoretical compositions can be attributed to the 5% excess of sodium acetate introduced during synthesis; partial decomposition and sublimation of this surplus acetate under calcination conditions likely led to a slight depletion of sodium in the final products.

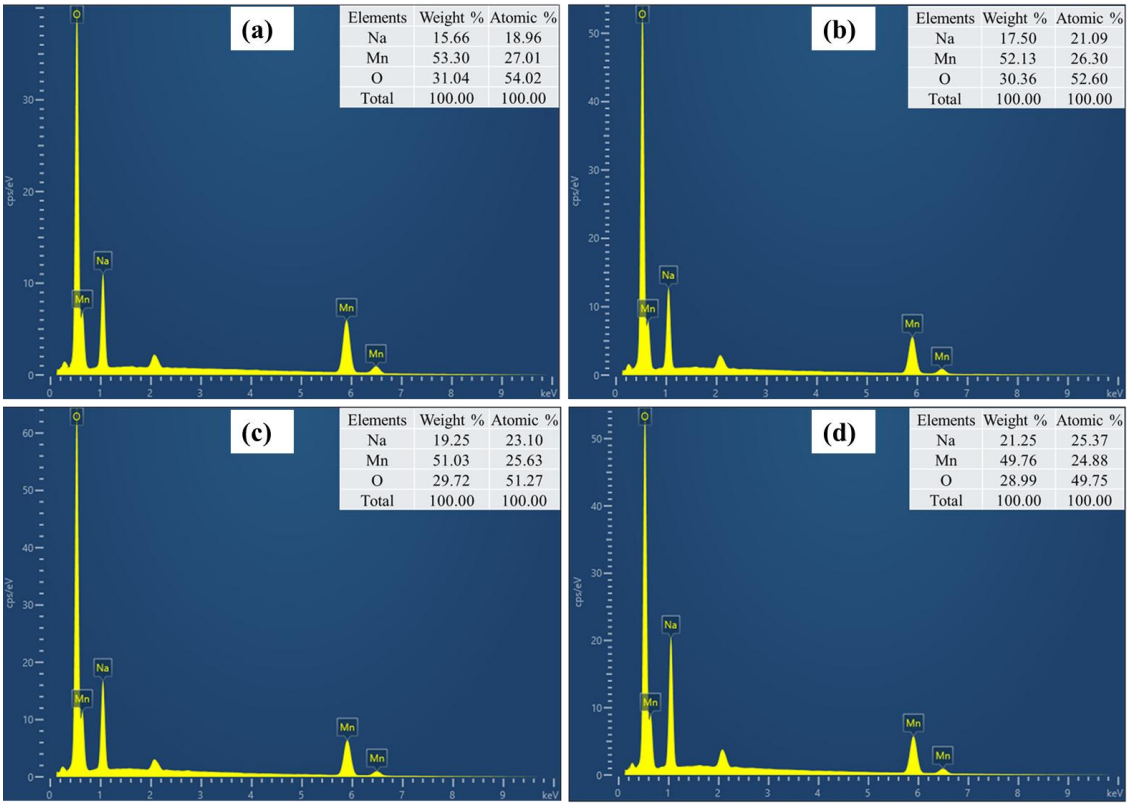

Fig. 3. Energy dispersive X-ray spectroscopy (EDX) results of α-Na_xMnO_2: (a) $Na_{0.7}MnO_2$; (b) $Na_{0.8}MnO_2$; (c) $Na_{0.9}MnO_2$; (d) $Na_{1.0}MnO_2$.

3.2. Electrochemical properties

The charging/discharging profiles for the first three cycles of Na_xMnO_2 at a current rate of 0.1 C are illustrated in Figs. 4a-d. As depicted, the specific charge/discharge capacities in the initial cycle for $Na_{0.7}MnO_2$, $Na_{0.8}MnO_2$, $Na_{0.9}MnO_2$, and $Na_{1.0}MnO_2$ are achieved at 156.65/152.61, 160.01/155.72, 162.15/158.20, and

168.44/165.18 $mAh.g^{-1}$, respectively. It is evident that the initial cycle capacities increase progressively with the Na:Mn ratio ranging from 0.7 to 1.0. In subsequent cycles, all samples exhibit a relatively rapid decline in specific capacity, as reflected in the increasing separation between charge and discharge curves shown in Figs. 4a–d. Among these, the $Na_{0.8}MnO_2$ sample demonstrated the most stable performance, retaining a discharge capacity of 145.23 $mAh.g^{-1}$ after three cycles, equivalent to 93.26% of its initial capacity. Conversely, $Na_{1.0}MnO_2$ exhibited the most significant capacity fade, with a discharge capacity of only 140 $mAh.g^{-1}$ in the third cycle, representing 84.98% of its original value.

Figures 4e and 4f illustrate the discharge capacity and retention of capacity over the first 50 cycles for Na_xMnO_2 materials. As shown in Figs. 4e and 4f, all samples exhibited a sharp decline in discharge capacity within the initial ten cycles. Specifically, after ten cycles, the discharge capacities for $Na_{0.7}MnO_2$, $Na_{0.8}MnO_2$, $Na_{0.9}MnO_2$, and $Na_{1.0}MnO_2$ were 113.41, 119.05, 117.98, and 116.82 $mAh.g^{-1}$, respectively, corresponding to 74.31%, 76.44%, 74.58%, and 70.72% of their original values. Among these, $Na_{0.8}MnO_2$ displayed the best capacity retention in the early stage. Likewise, after 50 cycles, the discharge capacities recorded are 90.85, 98.69, 87.86, and 82.62 $mAh.g^{-1}$, which correspond to 59.54%, 63.37%, 55.54%, and 50.02% of the initial capacities for $Na_{0.7}MnO_2$, $Na_{0.8}MnO_2$, $Na_{0.9}MnO_2$, and $Na_{1.0}MnO_2$, respectively. These results further affirm that $Na_{0.8}MnO_2$ possesses the highest cycling stability, while $Na_{1.0}MnO_2$ demonstrates the poorest cycling stability.

V. Sudarsanan and colleagues calculated the formation energies of intermediate Na_xMnO_2 phases during the charge/discharge cycling of α-$NaMnO_2$, showing that the sodium-deficient phase at x = 2/3 ($Na_{2/3}MnO_2$) in the O3-layered configuration has the lowest energy and is the most thermodynamically stable [26]. Consequently, during charge/discharge cycling, the material sample $Na_{1.0}MnO_2$ gradually loses sodium ions and transforms into the more sustainable O3-$Na_{2/3}MnO_2$ phase. This explains why $Na_{1.0}MnO_2$ initially exhibits the highest capacity, owing to its maximal sodium content, yet experiences the most rapid capacity fade: the continuous depletion of Na^+ drives the structure toward the lower-energy, sodium-vacant O3-$Na_{2/3}MnO_2$ phase. Moreover, the presence of sodium vacancies in O3-$Na_{2/3}MnO_2$ can make it prone to further phase transitions and collapse of the O3-layered framework, thereby undermining the cycling stability of $Na_{1.0}MnO_2$.

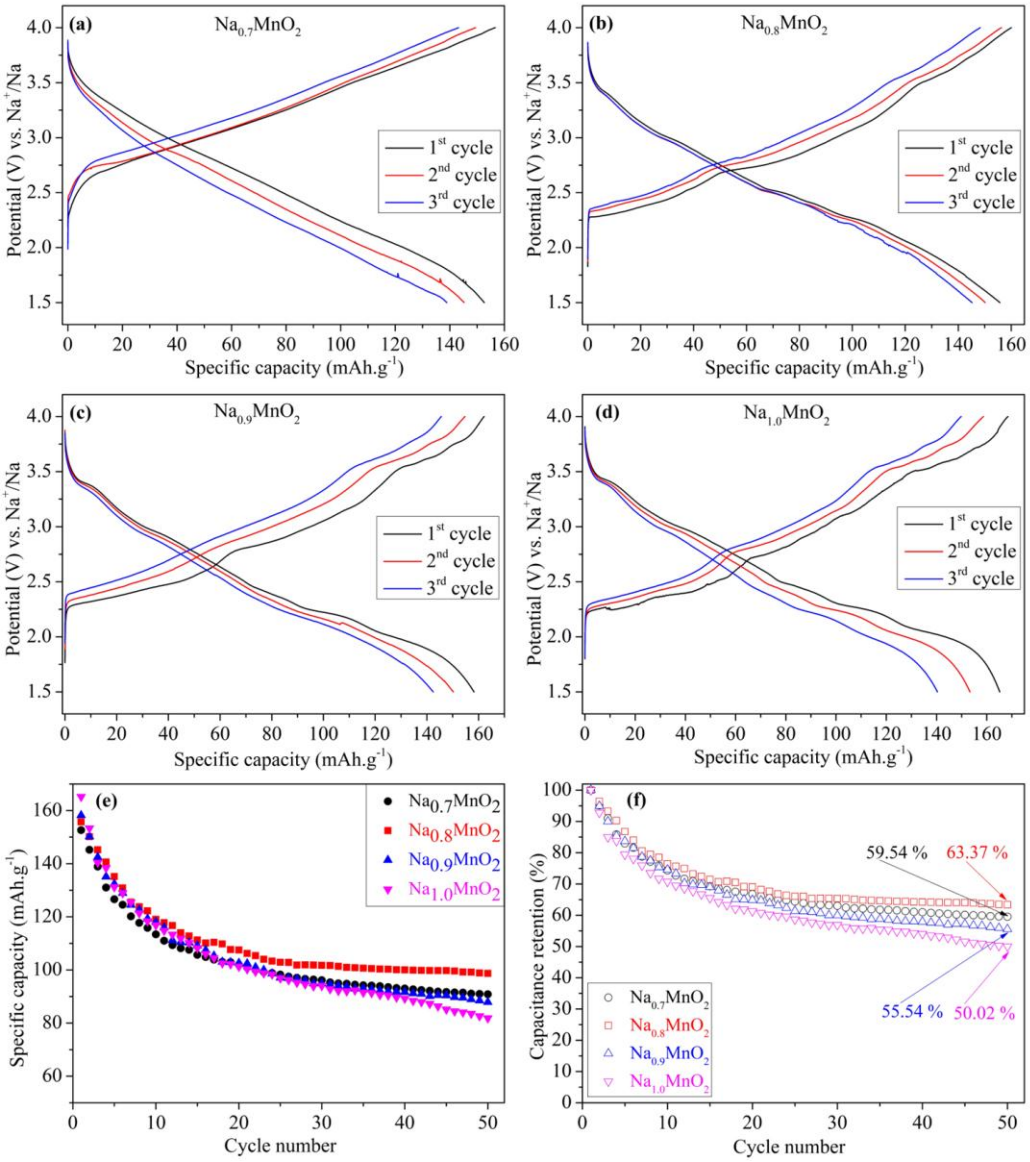

Fig. 4. (a, b, c, d) The charging/discharging profiles of the initial three cycles of Na_xMnO_2 at 0.1 C; (e, f) Cycling performance of Na_xMnO_2 in 50 cycles at 0.1 C.

The cycling stability of $Na_{0.7}MnO_2$ and $Na_{0.8}MnO_2$ exceeds that of $Na_{0.9}MnO_2$ and $Na_{1.0}MnO_2$, which can be explained by the inherently greater stability of the P2-type layered structure in α-$Na_{0.7}MnO_2$ compared to the O3-type layered structure of α-$NaMnO_2$ [17]. Moreover, the $Na_{0.8}MnO_2$ sample has a major phase composition of P2 of α-$Na_{0.7}MnO_2$, as shown in the XRD pattern in Fig. 1. The surplus Na^+ ions in the $Na_{0.8}MnO_2$ sample can occupy vacant octahedral sites in α-$Na_{0.7}MnO_2$, thereby boosting both its specific capacity and structural resilience. As a result, $Na_{0.8}MnO_2$ demonstrates the highest cycling stability among the series of Na_xMnO_2 materials.

Figure 5 presents the cyclic voltammetry (CV) scanning of Na_xMnO_2 samples. As illustrated in Fig. 5a, the CV curve of the $Na_{0.7}MnO_2$ sample exhibits a distinct pair of peaks at approximately 1.95 V and 3.25 V, which correspond to the redox reactions of the Mn^{4+}/Mn^{3+} couple during the charge-discharge process of the phase α-$Na_{0.7}MnO_2$ in the material [17], [24]. Additionally, a less pronounced pair of peaks appears at around 2.75 V and 3.85 V, which may be associated with the Mn^{4+}/Mn^{3+} redox couple originating from the minor phase in the $Na_{0.7}MnO_2$ material during cycling.

As shown in Fig. 5b, the CV curve of the $Na_{0.8}MnO_2$ sample reveals three relatively distinct oxidation peaks at approximately 2.75 V, 3.25 V, and 3.75 V, along with three corresponding reduction peaks observed at 3.35 V, 2.85 V, and 2.05 V. These three redox pairs may be associated with the Mn^{4+}/Mn^{3+} redox process occurring in the α-$Na_{0.7}MnO_2$ and α-$NaMnO_2$ phases, as well as the intermediate O3-$Na_{2/3}MnO_2$ phase of α-$NaMnO_2$. Additionally, the CV profile of the $Na_{0.8}MnO_2$ sample exhibits several subtle minor peaks, which could be related to the Mn^{4+}/Mn^{3+} redox couple of other intermediate phases.

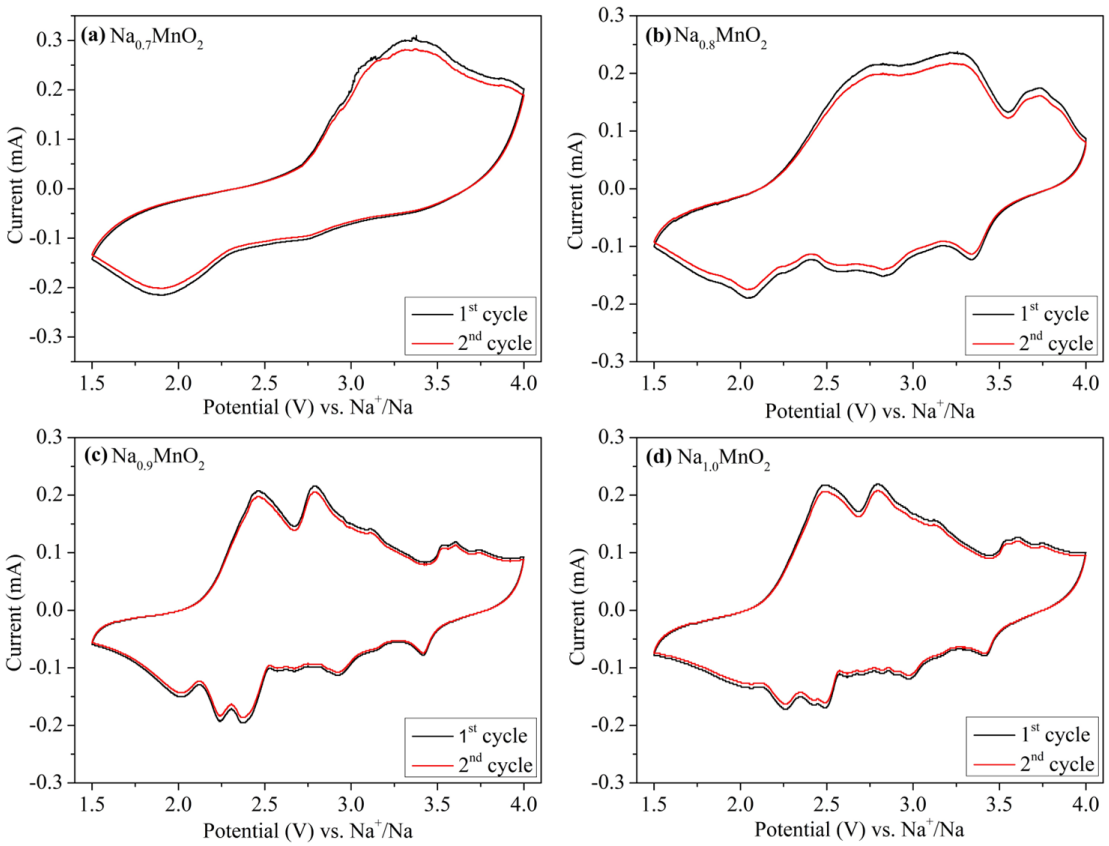

Fig. 5. The CV curves of Na_xMnO_2 at 0.1 mV. s^{-1}.

Similarly, Figs. 5c and 5d present the CV curves of the $Na_{0.9}MnO_2$ and $Na_{1.0}MnO_2$ samples. Both profiles exhibit two anodic peaks at 2.45 V and 2.75 V, and two cathodic peaks at 2.25 V and 2.45 V, which may be associated with the Mn^{4+}/Mn^{3+} redox reactions in the α-$NaMnO_2$ phase and the intermediate O3-$Na_{2/3}MnO_2$ phase of the $Na_{1.0}MnO_2$ sample during polarization. Additionally, both samples display a pair of peaks around 2.0 V and 3.2 V, potentially corresponding to the Mn^{4+}/Mn^{3+} redox behavior in the α-$Na_{0.7}MnO_2$ phase under cathodic and anodic polarization. Notably, this peak pair appears more prominent in the $Na_{0.9}MnO_2$ sample due to its higher content of α-$Na_{0.7}MnO_2$ compared to $Na_{1.0}MnO_2$, which is consistent with the XRD data. Furthermore, the CV curves of both samples contain minor peaks that may be related to the Mn^{4+}/Mn^{3+} redox couple of other intermediate phases during cycling.

Figure 6 shows the Nyquist plots of the Na_xMnO_2 samples. The results presented in Figs. 6a and 6b correspond to the samples before and after undergoing 50 charge/discharge cycles, respectively. As illustrated in Fig. 6, the impedance profiles of both before and after 50th cycling samples generally exhibit a semicircle representing the electrode's intrinsic resistance (Re), the charge-transfer resistance (Rct), and the double-layer capacitance (CPE), along with an inclined line in the low-frequency region, corresponding to Warburg impedance (Wo). The double-layer capacitance (CPE) includes CPEP constant phase element - porous (CPE_P) and constant phase element - transfer (CPE_T). The Warburg impedance (Wo) includes Warburg resistance (W_R), Warburg transmission line (W_T), and Warburg porous (W_P). The equivalent circuit diagram and the fitted component values were determined using ZPlot software, with the results shown in Fig. 6 and Tab. 2.

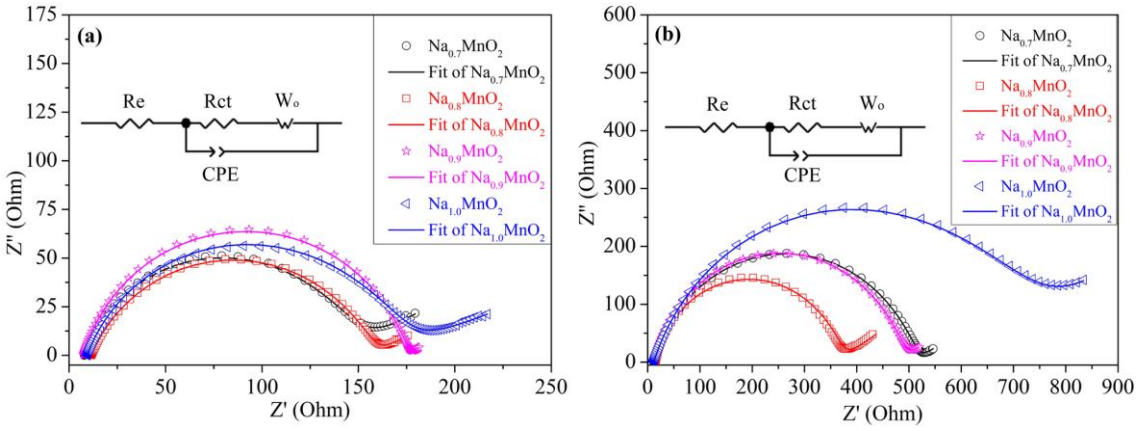

Fig. 6. Nyquist plots of the Na_xMnO_2 materials
(a) before cycle testing; (b) after 50th cycle testing.

Based on the results in Tab. 2 and the impedance spectra of the samples before cycling shown in Fig. 6a, the electrode resistance (Re) ranges from 7.8 Ω to 11.5 Ω, while the charge-transfer resistance (Rct) falls within 135 Ω to 168 Ω, demonstrating relatively minor variation among the samples. The lowest Rct value is observed in the $Na_{0.7}MnO_2$ sample, whereas $Na_{1.0}MnO_2$ shows the highest. In contrast, Fig. 6b and Tab. 2 reveal that the Rct values change significantly after 50 charge/discharge cycles, rising to 502 Ω, 352 Ω, 475 Ω, and 715 Ω for the $Na_{0.7}MnO_2$, $Na_{0.8}MnO_2$, $Na_{0.9}MnO_2$, and $Na_{1.0}MnO_2$ samples, respectively. Notably, the Rct of $Na_{1.0}MnO_2$ increased most substantially, by approximately 4.6 times compared to its pre-cycling value, whereas the $Na_{0.8}MnO_2$ sample experienced only a 2.4-fold increase. The increase in charge-transfer resistance after 50 charge/discharge cycles of the material samples increases the electrode polarization during charge/discharge. Therefore, it causes the voltage to increase rapidly during charge and decrease rapidly during discharge, leading to a decrease in the capacity of all samples. The $Na_{0.8}MnO_2$ sample has the least increase in charge transfer resistance after 50 charge/discharge cycles, so the capacity and cycling stability are the best. This result aligns well with the charge/discharge performance tests and explains why $Na_{0.8}MnO_2$ exhibits superior cycle stability compared to the other samples.

Tab. 2. Component values in the equivalent circuit diagram of Na_xMnO_2 samples before and after cycle testing

Before cycle testing				
Elements	$Na_{0.7}MnO_2$	$Na_{0.8}MnO_2$	$Na_{0.9}MnO_2$	$Na_{1.0}MnO_2$
Re (Ω)	8.01	11.5	7.8	9.35
R_{ct} (Ω)	135	144.5	168	155
CPE_T (F)	2×10^{-3}	3×10^{-4}	3×10^{-4}	5×10^{-4}
CPE_p	0.79	0.75	0.825	0.775
W_R (Ω)	0.1	0.075	0.008	0.35
W_T (F)	10^{-6}	10^{-6}	10^{-6}	10^{-7}
W_P	0.160	0.150	0.180	0.12
After cycle testing				
Elements	$Na_{0.7}MnO_2$	$Na_{0.8}MnO_2$	$Na_{0.9}MnO_2$	$Na_{1.0}MnO_2$
Re (Ω)	12.1	14.85	12.35	11.45
R_{ct} (Ω)	502	352	475	715
CPE_T (F)	2.8×10^{-4}	3×10^{-4}	8×10^{-4}	3×10^{-3}
CPE_p	0.815	0.865	0.85	0.785
W_R (Ω)	0.2	0.08	0.021	0.05
W_T (F)	6×10^{-5}	10^{-6}	10^{-6}	1.5×10^{-6}
W_P	0.180	0.185	0.2	0.22

4. Conclusion

The synthesized Na_xMnO_2 materials (x = 0.7-1.0) exhibited either a P2-type layered structure corresponding to α-$Na_{0.7}MnO_2$, as identified by JCPDS card #027-0751, or an O3-type layered structure corresponding to α-$NaMnO_2$, as identified by JCPDS card #025-0845. The sodium content during synthesis determined whether Na_xMnO_2 adopts the P2 or O3 phase; an increase in sodium content tends to favor the formation of the O3 phase. Morphological analysis revealed that the synthesized Na_xMnO_2 samples possess polyhedral shapes, with particle sizes ranging from one to several micrometers. Electrochemical characterization indicates that the $Na_{1.0}MnO_2$ sample achieved the highest initial charge/discharge capacity of 186.44/165.18 $mAh.g^{-1}$, while $Na_{0.7}MnO_2$ exhibited the lowest at 156.65/152.61 $mAh.g^{-1}$. All Na_xMnO_2 samples displayed rapid capacity degradation during early cycles. Notably, $Na_{1.0}MnO_2$ demonstrated the weakest cycling stability, retaining only 50.02% of its initial discharge capacity after 50 cycles. In contrast, $Na_{0.8}MnO_2$ maintained a discharge capacity of 98.69 $mAh.g^{-1}$ after 50 cycles, which corresponds to 63.37% of its initial value. $Na_{0.8}MnO_2$ shows strong promise as a cathode candidate for development in sodium-ion battery technology.

References

[1] J. Y. Hwang, S. T. Myung, and Y. K. Sun, "Sodium-ion batteries: Present and future", *Chemical Society Reviews*, Vol. 46, No. 12, pp. 3529-3614, 2017. DOI: 10.1039/c6cs00776g

[2] T. T. H. Nguyen, "Synthesis and electrochemical characteristics of zinc-doped sodium manganese oxide as a cathode material for sodium-ion batteries", *Journal of Science and Technique - Section on Physics and Chemical Engineering*, Vol. 1, No. 01, pp. 30-39, 2023. DOI: 10.56651/lqdtu.jst.v1.n01.623.pce

[3] V. K. Nguyen, V. N. Nguyen, and D. L. Vu, "Studying the electrochemical properties of potassium-doped sodium-manganese oxide cathode materials for sodium-ion batteries", *Journal of Science and Technique*, Vol. 2, No. 02, pp. 77-89, 2024. DOI: 10.56651/lqdtu.jst.v2.n02.862.pce

[4] T. P. Doan, N. T. Van, K. N. Van, Q. Q. Ngo, and T. N. Van, "Development of sodium-lithium-manganese-cobalt oxide with B doping or B/F dual doping as cathode electrode materials for sodium-ion batteries", *ACS Omega*, Vol. 9, Iss. 47, pp. 46916-46928, 2024. DOI: 10.1021/acsomega.4c06248

[5] N. Van Nghia *et al.*, "Synthesis and application of $NaNi_{0.5}Ti_{0.5}O_2$ as electrode material for sodium ion batteries", *VNU Journal of Science: Natural Sciences and Technology*, Vol. 38, No. 3, pp. 37-44, 2022.

[6] J. Parant, R. Olazcuaga, M. Devalette, C. Fouassier, and E. T. P. Hagenmuller, "Sur quelques nouvelles phases de formule Na_xMnO_2 (x<1)", *Journal of Solid State Chemistry*, Vol. 3, pp. 1-11, 1971.

[7] F. Yin *et al.*, "$Na_4Mn_9O_{18}$/carbon nanotube composite as a high electrochemical performance material for aqueous sodium-ion batteries", *Nanoscale Research Letters*, Vol. 12, pp. 1-9, 2017. DOI: 10.1186/s11671-017-2340-1

[8] R. Ruffo *et al.*, "Impedance analysis of $Na_{0.44}MnO_2$ positive electrode for reversible sodium batteries in organic electrolyte", *Electrochimica Acta*, Vol. 108, pp. 575-582, 2013. DOI: 10.1016/j.electacta.2013.07.009

[9] E. Hosono, T. Saito, J. Hoshino, M. Okubo, and Y. Saito, "High power Na-ion rechargeable battery with single-crystalline $Na_{0.44}MnO_2$ nanowire electrode", *Journal of Power Sources*, Vol. 217, pp. 43-46, 2012. DOI: 10.1016/j.jpowsour.2012.05.100

[10] B. Fu, X. Zhou, and Y. Wang, "High-rate performance electrospun $Na_{0.44}MnO_2$ nano fibers as cathode material for sodium-ion batteries", *Journal of Power Sources Journal*, Vol. 310, pp. 102-108, 2016. DOI: 10.1016/j.jpowsour.2016.01.101

[11] R. Ruffo *et al.*, "Impedance analysis of $Na_{0.44}MnO_2$ positive electrode for reversible sodium batteries in organic electrolyte", *Electrochimica Acta*, Vol. 108, pp. 575-582, 2013. DOI: 10.1016/j.electacta.2013.07.009

[12] X. He *et al.*, "Durable high-rate capability $Na_{0.44}MnO_2$ cathode material for sodium-ion batteries", *Nano Energy*, Vol. 27, pp. 602-610, 2016. DOI: 10.1016/j.nanoen.2016.07.021

[13] J. Y. J. Y. Li *et al.*, "Identifying the critical role of Li substitution in P2-$Na_x[Li_yNi_zMn_{1-y-z}]O_2$ ($0 < x, y, z < 1$) intercalation cathode materials for high-energy Na-ion batteries", *Chemistry of Materials*, Vol. 26, pp. 1260-1269, 2014. DOI: 10.15242/iie.e0314110

[14] J. Zhang and D. Y. W. Yu, "Stabilizing $Na_{0.7}MnO_2$ cathode for Na-ion battery via a single-step surface coating and doping process", *Journal of Power Sources*, Vol. 391, pp. 106-112, 2018. DOI: 10.1016/j.jpowsour.2018.04.077

[15] D. Sohn *et al.*, "Fabrication of $Na_{0.7}MnO_2$/C composite cathode material by simple heat treatment for high-power Na-ion batteries", *Electronic Materials Letters*, Vol. 14, No. 1, pp. 30-36, 2018. DOI: 10.1007/s13391-017-7085-6

[16] T. Sun *et al.*, "Micron-sized $Na_{0.7}MnO_{2.05}$ as cathode materials for aqueous rechargeable magnesium-ion batteries", *International Journal of Ionics - The Science and Technology of Ionic Motion*, Vol. 25, pp. 4805-4815, 2019.

[17] M. A. Khan, D. Han, G. Lee, Y. Il Kim, and Y. M. Kang, "P2/O3 phase-integrated $Na_{0.7}MnO_2$ cathode materials for sodium-ion rechargeable batteries", *Journal of Alloys and Compounds*, Vol. 771, pp. 987-993, 2019. DOI: 10.1016/j.jallcom.2018.09.033

[18] T. H. N. Thi *et al.*, "Co and F co-doping to augmenting the electrochemical performance of P2-type sodium lithium manganese oxide for sodium ion battery", *Journal of Electroanalytical Chemistry*, Vol. 972, 2024. DOI: 10.1016/j.jelechem.2024.118590

[19] D. Nayak, P. Kumar, S. Ghosh, and V. Adyam, "Aluminium substituted β-type $NaMn_{1-x}Al_xO_2$: A stable and enhanced electrochemical kinetic sodium-ion battery cathode", *Journal of Power Sources*, Vol. 438, 2019. DOI: 10.1016/j.jpowsour.2019.227025

[20] L. Zhang, Y. Zhang, Z. Su, H. Tian, and L. Wang, "Synthesis and electrochemical characterization of α-$NaMnO_2$ as a cathode material for hybrid Na/Li-ion batteries", *International Journal of Electrochemical Science*, Vol. 14, pp. 2422-2429, 2019. DOI: 10.20964/2019.03.82

[21] J. Billaud *et al.*, "β-$NaMnO_2$: A high performance cathode for sodium-ion batteries", *Journal of the American Chemical Society*, Vol. 136, Iss. 49, pp. 1-9, 2014. DOI: 10.1021/ja509704t

[22] R. J. Clément, D. S. Middlemiss, I. D. Seymour, A. J. Ilott, and C. P. Grey, "Insights into the nature and evolution upon electrochemical cycling of planar defects in the β-$NaMnO_2$ Na-ion battery cathode: An NMR and first-principles density functional theory approach", *Chemistry of Materials*, Vol. 28, pp. 8228-8239, 2016. DOI: 10.1021/acs.chemmater.6b03074

[23] K. Kubota *et al.*, "Structural change induced by electrochemical sodium extraction from layered O'3-$NaMnO_2$", *Journal of Materials Chemistry A*, Vol. 9, pp. 26810-26819, 2021. DOI: 10.1039/d1ta05390f

[24] Q. Meng *et al.*, "Regulation of P2/O3 layered-oxide cathode by cation potential and dual-site doping provides excellent electrochemical performance", *Journal of Colloid and Interface Science*, Vol. 691, 2025. DOI: 10.1016/j.jcis.2025.137437

[25] L. Zhang, Y. Zhang, Z. Su, H. Tian, and L. Wang, "Synthesis and electrochemical characterization of α-$NaMnO_2$ as a cathode material for hybrid Na/Li-ion batteries", *International Journal of Electrochemcal Science*, Vol. 14, No. 3, pp. 2422-2429, 2019. DOI: 10.20964/2019.03.82

[26] V. Sudarsanan, A. M. Augustine, C. Vivek, and P. Ravindran, "Ab-initio based thermodynamic study on α-$NaMnO_2$ for Na-ion battery applications", *AIP Conference Proceedings*, Vol. 2115, Iss. 1, 2019.

ĐẶC TÍNH ĐIỆN HÓA CỦA VẬT LIỆU CATỐT α-Na_xMnO_2 ỨNG DỤNG CHO PIN NATRI-ION

Nguyễn Văn Kỳ[1,2], Vũ Đình Thảo[1], Lương Trung Sơn[1],
Vũ Đình Lãm[2], Nguyễn Văn Nghĩa[3]

[1]*Khoa Hóa - Lý kỹ thuật, Trường Đại học Kỹ thuật Lê Quý Đôn*

[2]*Học viện Khoa học và Công nghệ, Viện Hàn lâm Khoa học và Công nghệ Việt Nam*

[3]*Viện Kiến trúc, Xây dựng, Đô thị và Công nghệ, Trường Đại học Kiến trúc Hà Nội*

Tóm tắt: Vật liệu cấu trúc lớp P2 và O3 có tiềm năng lớn để ứng dụng làm cực dương cho pin ion natri. Bài báo trình bày kết quả nghiên cứu về tính chất điện hóa của vật liệu catốt cấu trúc lớp α-Na_xMnO_2 (x = 0,7-1,0) được tổng hợp bằng phương pháp sol-gel. Vật liệu catốt α-Na_xMnO_2 được đặc trưng bằng phương pháp nhiễu xạ tia X (XRD) để xác định cấu trúc tinh thể, kính hiển vi điện tử quét (SEM) để phân tích hình thái và phổ tia X tán xạ năng lượng (EDX) để đánh giá thành phần các nguyên tố. Tính chất điện hóa của vật liệu α-Na_xMnO_2 đã được nghiên cứu bằng cách sử dụng pin cúc áo CR2032, trong đó catốt được chế tạo từ vật liệu α-Na_xMnO_2 tổng hợp được. Vật liệu catốt α-Na_xMnO_2 thể hiện dung lượng nạp/xả ban đầu cao nhất ở tốc độ 0,1 C khi x = 1,0, với các giá trị lần lượt là 168,43 mAh.g^{-1} và 165,18 mAh.g^{-1} trong chu kỳ đầu tiên. Tuy nhiên, dung lượng giảm đáng kể sau 10 chu kỳ và chỉ đạt khoảng 50,02% giá trị ban đầu sau 50 chu kỳ. Mẫu vật liệu có độ ổn định chu kỳ cao nhất là $Na_{0,8}MnO_2$ (x = 0,8), duy trì 63,37% dung lượng ban đầu sau 50 chu kỳ. Các phép đo phổ tổng trở điện hóa (EIS) và quét thế vòng tuần hoàn (CV) đã được thực hiện bằng cách sử dụng máy đo điện hoá đa năng IVIUM để đánh giá các tính chất điện hóa của các vật liệu tổng hợp được. Vật liệu α-Na_xMnO_2 thể hiện tiềm năng triển vọng như một ứng cử viên catốt cho pin natri-ion.

Từ khóa: *Pin natri-ion; natri mangan oxit; vật liệu catốt; phương pháp sol-gel.*

Received: 19/07/2025; Revised: 20/09/2025; Accepted for publication: 29/10/2025

❑